

ARTICLE TYPE

Prediction of multiphase flows with sharp interfaces using anisotropic mesh optimisation

Asiri Obeysekara^{*1,2} | Pablo Salinas¹ | Claire E. Heaney¹ | Lyes Kahouadji^{1,2} | Lluís Via-Estrem¹ | Jiansheng Xiang¹ | Narakorn Srinil³ | André Nicolle⁴ | Omar K. Matar² | Christopher C. Pain¹

¹Applied Modelling and Computation Group, Department of Earth Science and Engineering, Imperial College London, Prince Consort Road, SW7 2AZ London, U.K.

²Department of Chemical Engineering, Imperial College London, Prince Consort Road, SW7 2AZ, London, U.K.

³School of Engineering, Newcastle University, Newcastle upon Tyne, U.K.

⁴AMT group, BP PLC, Sunbury-upon-Thames, U.K.

Correspondence

*Asiri Obeysekara, Email: a.obeysekara@imperial.ac.uk

Present Address

Royal School of Mines, Prince Consort Road, Imperial College London, U.K.

Summary

We propose an integrated, parallelised modelling approach to solve complex multiphase flow problems with sharp interfaces. This approach is based on a finite-element, double control-volume methodology, and employs highly-anisotropic mesh optimisation within a framework of methods and features. Each method is integral to increasing the fidelity of representing the underlying physics while maximising computational efficiency. We validate our numerical predictions against standard benchmark literature results and demonstrate capabilities of our modelling framework via simulation of laminar and turbulent two-phase pipe flows. These complex interfacial flows involve the creation of bubbles and slugs, which involve multi-scale physics and arise due to a delicate interplay amongst inertia, viscous, gravitational, and capillary forces. We also comment on the potential use of our integrated approach to simulate large, industrial-scale multiphase pipe flow problems that feature complex topological transitions.

KEYWORDS:

flow, finite-element, adaptivity, turbulence, multiphase, slug flow

1 | INTRODUCTION

Multiphase flow in a pipe can be characterised by the configuration or flow pattern of the phases involved. Generally, the interaction is the result of the material properties, and the initial and input parameters of the phases (such as the superficial velocities at the inlets), alongside geometrical constraints (diameter, length, bend radii) of the pipe configuration¹. The strong coupling of the mechanisms arising in such systems generally governs the physics of the flow dynamics²; turbulence, gravity, viscous forces, coupling between the phases, as well as density- and shear-driven instabilities include a few of the mechanisms that are present. Phenomena such as interfacial waves, bubble and drop creation, breakup, coalescence, deposition and entrapment directly contribute to the emergence of wide range of complex flow patterns in multiphase pipe flow. In the present work, we will focus on gas-liquid pipe flows.

Slug flow, characterised by the sequences of liquid ‘slugs’ separated by regions containing dispersed bubbles, is of particular interest to many industrial processes (such as oil and gas extraction, pipeline transportation, and geothermal production)³ due to the wide range of gas-liquid flow rates at which slug flow has been observed. The flow regime transients that lead to the slug flow generation and evolution in pipes have received considerable attention in the literature^{3,4,5} though a number of open problems

⁰**Abbreviations:** CFD, computational fluid dynamics; DCV, double control volume; HPC, high-performance computing; VOF, volume-of-fluid

have remained hitherto unresolved. For instance, due to the inherent unsteadiness and intermittency of the flow, Omebere-Iyar *et al.*⁶ observed that slug flow in vertical pipes can be particularly challenging to predict with a ‘classical’ approach.

More generally, accurate prediction of slug flow characteristics, such as slug length and frequency, via full-scale numerical simulations is challenging due to the interactions of the turbulent gas and liquid phases, which lead to complex interfacial topological transitions. The turbulence present in these systems gives rise to a large range of spatial and temporal scales that require an array of robust and accurate numerical methods to capture the emergent physical phenomena arising particularly in industrially-relevant flows. Many Computational Fluid Dynamics (CFD) tools have been developed to capture these phenomena⁷. In order to model the interface, there are predominantly three methods in common usage: interface-capturing techniques of which Volume-Of-Fluid (VOF) methods are prime exemplars^{2,7,8,9,10}, interface-tracking methods (see the work of Shin *et al.*¹¹ and references therein), and phase-field methods (see Soligo *et al.*¹² and references therein); we adopt the interface-capturing approach in this paper.

It is also important to capture surface tension driven phenomena with associated sub-grid scale physics, which may require the adoption of hybrid strategies. Herrmann¹³ demonstrated the use of explicit filtering and ‘Refined Level-Set’ method to resolve a sub-grid interface on an auxiliary grid and solve for surface tension terms of the Navier-Stokes equations. The development of a single modelling framework, which encompasses as many of the relevant methods for accurate, reliable, and efficient simulation of complex multiphase flows and associated regime transitions is therefore of crucial importance but poses significant challenges. The use of dynamic and anisotropic mesh-adaptivity to provide increased resolution where required in the flow and computational domain could provide the bedrock for the creation of such a framework.

In this paper, we describe the development of an integrated modelling framework for multiphase pipe-flows that can exploit a range of physics-capturing/resolving numerical schemes, which are listed in Table 1. This framework relies on the use of hydrostatic and surface tension force balancing models, mesh-adaptivity, massive parallelisation, and high-performance computing. The use of the ‘Double-Control Volume’ (DCV) method as the basis of the framework, first introduced by¹⁴ for porous media flow, permits the deployment of highly-anisotropic unstructured mesh elements with adaptive mesh optimisation, while ensuring solution stability. It has already been demonstrated by¹⁵ for free surface inertia-dominated flows in the context of numerical wave-tanks that the total number of adaptive mesh elements is reduced significantly (by up to two orders of magnitude) when using DCV methods.

In the context of multiphase pipe-flows, forming an initial mesh with *a posteriori* knowledge of the internal flow is unnecessary, and complex topography of gas-liquid interfaces can be well represented, thereby increasing computational efficiency alongside model accuracy. The methods described in this paper enable the simulation of multiphase flows in a wide range of settings including porous-media flow^{16,17}, fluid-solid coupling^{18,19}, and interfacial flows^{2,10,20}. Here, we present the formulation and validation of the balanced-force, high-order accurate and efficiency maximising methods within a new open-source, integrated parallel framework, for modelling complex multiphase flows in high-aspect ratio domains.

The rest of the paper is organised as follows: Section 2 presents the governing equations for incompressible flow and their discretisation, alongside descriptions of the numerical methods used to capture complex multiphase flow in pipes integrated within the framework. Validation of the framework, and numerical examples of Taylor bubbles and free-bubbling flow, are presented in Section 3. Finally, a discussion is presented in Section 4, and concluding remarks are in Section 5.

2 | GOVERNING EQUATIONS, DISCRETISATION AND SOLUTION

2.1 | Governing equations

For multi-component flow modelling, one phase is generalised into an arbitrary number of components¹⁰. If α_i is the volume fraction of component i , and N_c is the number of components, where $i = 1, 2, 3, \dots, N_c$, then a constraint of the system as

$$\sum_{i=1}^{N_c} \alpha_i = 1 \quad (1)$$

is used to define the conservation of mass for each component i as

$$\frac{\partial}{\partial t}(\alpha_i \rho_i) + \nabla \cdot (\alpha_i \rho_i \mathbf{u}) - Q_i = 0, \quad i = 1, 2, 3, \dots, N_c \quad (2)$$

TABLE 1 Modelling features and aims embedded within the generalised fluid dynamics solver IC-FERST for modelling steady and unsteady multiphase flow in pipes (relevant section numbers are given in parentheses.)

Modelling features	Aims
(A) Spatial adaptive mesh optimisation with domain decomposition of large domains for parallel computations	Multi-scale resolution of what is important to resolve in serial and parallel simulations (2.4.5)
(B) Conservative-Galerkin mesh-to-mesh interpolation	Conservation of mass and other properties and accurate interpolation (2.4.5)
(C) Combined Finite-Element (FE) and ‘Double Control-Volume’ (DCV) methods	Ladyzhenskaya–Babuška–Brezzi (LBB) stability and accuracy on meshes with poor elements in high-aspect ratio domains (2.3)
(D) Petrov-Galerkin and Discontinuous-Galerkin (DG) for velocity and implicit Large-Eddy Simulations (LES)	Accuracy and stability for modelling of turbulence and momentum (2.4.3)
(E) Hydrostatic pressure solver	Accurate hydrostatic pressure and buoyancy balance solutions with quadratic piece-wise elements (2.4.4)
(F) Implicit discretisation in time, adaptive time-step	Ensure/Maintain the accuracy with large time-steps and Courant numbers (2.2)
(G) Projecting solutions to a system that satisfies the governing equations after changing the mesh	Equation balances preserved after mesh optimisation (2.4.1)
(H) Metric advection of resolution	Prediction of where mesh resolution is needed at future times (2.4.6)
(I) Positivity preserving high-order flux limiting in space and time, including compressive advection interface capturing	Physical realism, accuracy and maintaining sharp interfaces during modelling multiphase flows (2.2), (2.4.2)
(J) Weak boundary conditions	Improving formal accuracy of numerical solution at boundaries
(L) Linear solvers - algebraic multi-grid pressure and modified velocity Jacobi preconditioners using PETSc	Rapid linear solver convergence and reliability

where ρ_i , t , \mathbf{u} , Q_i is the density of component i , time, velocity and mass source term, respectively. The equation of motion, assuming an incompressible viscous fluid, may be written as

$$\frac{\partial(\rho \mathbf{u})}{\partial t} + \nabla \cdot (\rho \mathbf{u} \otimes \mathbf{u}) = -\nabla p + \nabla \cdot [\mu(\nabla \mathbf{u} + \nabla^T \mathbf{u})] + \rho \mathbf{g} + \mathbf{F}_\sigma \quad (3)$$

where ρ is the bulk density defined as $\rho = \sum_{i=1}^{N_c} \alpha_i \rho_i$, p is the pressure, $\mu = \sum_{i=1}^{N_c} \alpha_i \mu_i$ is the bulk dynamic viscosity, \mathbf{g} is the gravitational acceleration vector, and \mathbf{F}_σ is the surface tension force balance. The surface tension model is a balance force algorithm of the Continuum Surface Force method (CSF)²¹ and is defined as

$$\mathbf{F}_\sigma = \sigma \kappa \tilde{\mathbf{n}} \delta \quad (4)$$

where σ is the surface tension coefficient, κ is the interfacial curvature, $\tilde{\mathbf{n}}$ is the outward-pointing interface unit normal, and δ is the Dirac delta function.

2.2 | Temporal discretisation

The explicit Forward-Euler first-order time-stepping scheme is commonly used due to its simplicity though the time-step size is constrained by the Courant-Friedrichs-Lewy condition (CFL). Although implicit methods are able to use larger time-steps, they do introduce numerical diffusion which could artificially smooth any interfaces present. For stability and accuracy of all solutions, an adaptive- θ method has been adopted, which can represent the forward Euler method for $\theta = 0$, the backward Euler method for $\theta = 1$, and the Crank-Nicholson scheme is obtained for $\theta = 0.5$. Keeping the θ value close to zero ensures the interface remains as sharp as possible^{10,21,22}.

2.3 | Spatial discretisation

In order to discretise the governing Equations (2) and (3), a triangle/tetrahedral finite-element representation for velocity \mathbf{u} , and control-volume representation for pressure p is assumed, as shown in Figure 1. The discretisation of velocity with \mathcal{N} discontinuous piecewise-linear (P1_{DG}) degrees-of-freedom and the pressure field with \mathcal{M} control-volumes¹⁴ can be expressed in terms of their finite-element basis functions N_j and control-volume basis function M_j , respectively:

$$\mathbf{u} = \sum_{j=1}^{\mathcal{N}} \mathbf{u}_j \mathbf{N}_j \quad \text{and} \quad p = \sum_{j=1}^{\mathcal{M}} p_j M_j, \quad (5)$$

where the number of nodes \mathcal{N} in the FEM representation, and the number of control-volumes \mathcal{M} are not necessarily equal. The matrix \mathbf{N}_j contains the basis functions and can be written as $\mathbf{N}_j = N_j \mathbf{I}$, where \mathbf{I} is the identity matrix and N_j is the j th finite-element basis function.

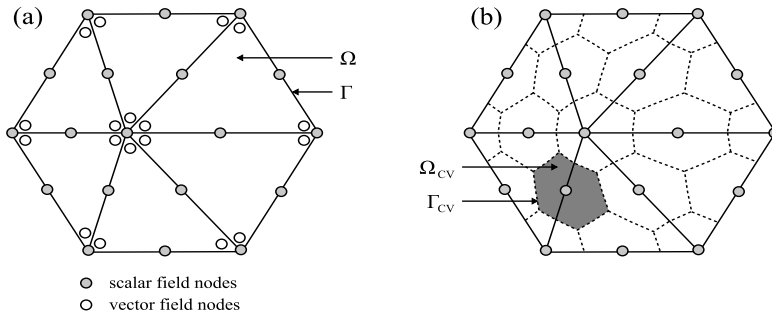


FIGURE 1 (a) Example of discretisation scheme used in formulation involving P1_{DG}-P2 elements²³. Shaded nodes represent degrees-of-freedom for the continuous fields (in this example, the representation is quadratic piece-wise P2) whilst white nodes represent degrees-of-freedom for the vector field (i.e. discontinuous linear piece-wise P1_{DG} for velocity \mathbf{u}). Ω is the volume of the domain and Γ is its bounding surface. (b) Control volumes of the same P2 elements, outlined by dashed lines. Ω_{cv} is the volume of the control volume and Γ_{cv} is its bounding surface. Image taken from Cotter *et al.*²³.

The continuity equation, Eq. (2), is discretised using a control-volume basis function M_j and applying integration by parts to each control-volume j ^{10,14,22}. The time-discretisation for the multi-component terms are carried out using forward-Euler for the reasons described in Section 2.2, and adaptive- θ for the advection terms in Equation (2) to yield the discretised form of global continuity:

$$\int_{V_m} M_j \left(\frac{\alpha_{im}^{n+1} \tilde{\rho}_{im}^{n+1} - \alpha_{im}^n \rho_{im}^n}{\Delta t} \right) dV + \int_{\Gamma_{V_m}} \left[\theta_{im}^{n+\frac{1}{2}} \hat{\alpha}_{im}^{n+1} \hat{\rho}_{im}^{n+1} \mathbf{n} \cdot \mathbf{u}^{n+1} + \left(1 - \theta_{im}^{n+\frac{1}{2}} \right) \hat{\alpha}_{im}^n \hat{\rho}_{im}^n \mathbf{n} \cdot \mathbf{u}^n \right] d\Gamma = 0, \quad i = 1, 2, 3, \dots, \mathcal{M}, \quad (6)$$

where \mathbf{n} is the unit normal vector point outwards from the surface Γ_{V_m} of the control-volume V_m , Δt is the time-step, $\theta \in \{0, 1\}$ is the implicitness parameter from the adaptive- θ method, n is the current time-level. The variables denoted with a *hat* ($\hat{\cdot}$) and *tilde* ($\tilde{\cdot}$) represent flux-limited and latest values of the variable, respectively. More details on the flux-limiting scheme are presented in Section 2.4.2.

To yield the discrete form of the momentum equation, Equation (3) is tested with a linear DG basis function and θ time-discretisation as

$$\begin{aligned} \int_{V_E} \mathbf{N}_j \left(\frac{\partial(\rho \mathbf{u})}{\partial t} + \nabla \cdot (\rho \mathbf{u} \otimes \mathbf{u}) + \nabla p - \nabla \cdot [\mu(\nabla \mathbf{u} + \nabla^T \mathbf{u})] - \rho \mathbf{g} - \mathbf{F}_\sigma \right) dV \\ \approx \int_{V_E} \mathbf{N}_j \left(\frac{\rho(\mathbf{u}^{n+1} - \mathbf{u}^n)}{\Delta t} + \nabla p^{n+1} - \rho \mathbf{g} - \mathbf{F}_\sigma \right) dV \\ + \theta(\mathbf{S}_{jADV}^{n+1} + \mathbf{S}_{jVIS}^{n+1}) + (1 - \theta)(\mathbf{S}_{jADV}^n + \mathbf{S}_{jVIS}^n) \\ + \int_{\Gamma_{bc}} \mathbf{N}_j \hat{\mathbf{n}} (p_{bc}^{n+1} - p^{n+1}) d\Gamma = \mathbf{0} \end{aligned} \quad (7)$$

where $\hat{\mathbf{n}}$ is the unit normal vector point outwards from the surface Γ_E of the element V_E , Γ_{bc} is a boundary with a prescribed pressure condition, and \mathbf{S}_{jADV} and \mathbf{S}_{jVIS} represent the discrete form of the advection and viscous terms, respectively²¹.

An upwind DG method for the advection term \mathbf{S}_{jADV} at $n+1$ is given by

$$\mathbf{S}_{jADV}^{n+1} = \int_{V_E} \rho \mathbf{N}_j \mathbf{u}_*^{n+1} \cdot \nabla \mathbf{u}^{n+1} dV - \int_{\Gamma_E} \rho \mathbf{N}_j \mathbf{u}_*^{n+1} \mathbf{n} \cdot (\mathbf{u}^{n+1} - \mathbf{u}_{in}^{n+1}) d\Gamma \quad (8)$$

where \mathbf{u}_{in} is the upwind velocity calculated from neighbouring element, and the subscript (*) represents the latest value during an iteration of one time step. A high-order linear scheme for the viscous term \mathbf{S}_{jVIS} at $n+1$ is obtained by using a high-order linear scheme for the viscous terms $\boldsymbol{\tau} = \mu(\nabla \mathbf{u} + \nabla^T \mathbf{u})$ such as

$$\mathbf{S}_{jVIS}^{n+1} = \int_{V_E} \nabla \cdot \mathbf{N}_j : \boldsymbol{\tau}^{n+1} dV - \frac{1}{2} \int_{\Gamma_E} \mathbf{N}_j \boldsymbol{\tau}_{nb}^{n+1} d\Gamma \quad (9)$$

where $\boldsymbol{\tau}_{nb}$ is the value of $\boldsymbol{\tau}$ in the neighbouring elements along the face.

2.4 | Numerical methods for modelling multiphase flow

2.4.1 | Projection of solutions

The discretised continuity equation and momentum equations, given by Eqs. (6) and (7), are written in matrix form for time $n + 1$, respectively, as

$$(\mathbf{M}_u + \mathbf{A}) \underline{\mathbf{u}}^{n+1} = \mathbf{C} \underline{\mathbf{p}}^{n+1} + \underline{\mathbf{s}}_u^{n+1} \quad (10)$$

$$\mathbf{M}_p \underline{\mathbf{p}}^{n+1} + \mathbf{B}^T \underline{\mathbf{u}}^{n+1} = \underline{\mathbf{s}}_p^{n+1} \quad (11)$$

where $\underline{\mathbf{u}}^{n+1}$ and $\underline{\mathbf{p}}^{n+1}$ are the FEM solutions for velocity and pressure, respectively, and $\underline{\mathbf{s}}_u^{n+1}$ and $\underline{\mathbf{s}}_p^{n+1}$ are the discretised source terms^{10,21}. Matrix \mathbf{A} contains terms relating to the implicit treatment of the velocity. Although sparse, this matrix does not have a block-diagonal structure and therefore is not easily inverted. The global mass balance, Eq. (11), and force balance, Eq. (10), are solved here by using a projection method, which effectively eliminates the velocity and solves a system of equations for the pressure or pressure correction. Using the discontinuous velocity within an element formulation, the matrix \mathbf{M}_u is block-diagonal and thus easily invertible, with each block being local to an element^{21,10}. This allows the method to be applied to both inertia- and viscous-dominated flows without modification.

The solution method proceeds by first solving for an intermediate velocity $\underline{\mathbf{u}}_*^{n+1}$ using a guessed pressure $\underline{\mathbf{p}}_*^{n+1}$. One may use $\underline{\mathbf{p}}_*^{n+1} = \underline{\mathbf{p}}^n$ on the first iteration within a time step:

$$(\mathbf{M}_u + \mathbf{A}) \underline{\mathbf{u}}_*^{n+1} = \mathbf{C} \underline{\mathbf{p}}_*^{n+1} + \underline{\mathbf{s}}_u^{n+1}. \quad (12)$$

The matrix equation for velocity to be satisfied is:

$$\mathbf{M}_u \underline{\mathbf{u}}^{n+1} + \mathbf{A} \underline{\mathbf{u}}_*^{n+1} = \mathbf{C} \underline{\mathbf{p}}^{n+1} + \underline{\mathbf{s}}_u^{n+1}. \quad (13)$$

Subtracting Eq. (12) from Eq. (13), the velocity correction equation is obtained:

$$\mathbf{M}_u (\underline{\mathbf{u}}^{n+1} - \underline{\mathbf{u}}_*^{n+1}) = \mathbf{C} (\underline{\mathbf{p}}^{n+1} - \underline{\mathbf{p}}_*^{n+1}). \quad (14)$$

Multiplying Eq. (14) by $\mathbf{B}^T \mathbf{M}_u^{-1}$, and using the global continuity equation, Eq. (11), to eliminate $\underline{\mathbf{u}}^{n+1}$, one obtains the pressure correction equation:

$$(\mathbf{B}^T \mathbf{M}_u^{-1} \mathbf{C} + \mathbf{M}_p)(\underline{\mathbf{p}}^{n+1} - \underline{\mathbf{p}}_*^{n+1}) = -\mathbf{M}_p \underline{\mathbf{p}}_*^{n+1} - \mathbf{B}^T \underline{\mathbf{u}}_*^{n+1} + \underline{\mathbf{s}}_p^{n+1}. \quad (15)$$

This equation is solved for the pressure $\underline{\mathbf{p}}^{n+1}$ and the velocity is corrected using Eq. (12). The pressure is solved using Portable, Extensible Toolkit for Scientific computation (PETSc)²⁴, generalised minimal residual method (GMRES) Krylov subspace solver²⁵ and HYPRE's Boomer Algebraic Multi-Grid method (BoomerAMG) library for preconditioning²⁶. The velocity solutions are calculated using GMRES and a point-Jacobi preconditioner with a row-max scaling (i.e. with diagonal scaling using the maximum entry of each row) through PETSc.

2.4.2 | Compressive advection and interface capturing

A compressive advection method based on an interface-capturing scheme is employed here, with further development of the scheme to improve the sharpness of the interface described. The interface-capturing technique uses a Petrov-Galerkin method for capturing the interface; mass-conservation is solved using a control-volume and finite-element formulation, to obtain fluxes on the boundaries of the control-volumes, which are subject to flux-limiting using a Normalised Variable Diagram (NVD) approach^{10,21}. For interface capturing, the normalised interface value is limited based on NVD as in¹⁰:

$$\tilde{\varphi}_f = \begin{cases} \min \left\{ \max \left\{ \frac{1}{\tilde{\gamma} C}, \tilde{\gamma} \right\} \varphi_c, \max\{0, \varphi_f\} \right\}, & \text{if } \varphi_c \in (0, 1) \\ \varphi_c & \text{otherwise} \end{cases} \quad (16)$$

where the parameter $\tilde{\gamma}$ controls the 'compressiveness' of the applied scheme. The Courant number $C = \Delta t |\mathbf{u} \cdot \mathbf{n}| / h_{cd}$ is obtained from the velocity component normal to the face and the distance h_{cd} between the centroids of the current and downwind CVs. In this formulation, φ_f is the non-dimensional high-order face value:

$$\varphi_f = \frac{\phi_f - \phi_u}{\phi_d - \phi_u} \in [0, 1] \quad (17)$$

where ϕ_f is the high-order face value, ϕ_u and ϕ_d are the upwind and downwind face values, respectively (see Figure 2), and φ_c is the non-dimensional upwind face value defined as:

$$\varphi_c = \frac{\phi_c - \phi_u}{\phi_d - \phi_u} \in [0, 1] \quad (18)$$

Using upwind and downwind values, the compressive advection interface-capturing scheme can be extended to compress the interface further. This is implemented by extrapolating the far-field downwind value as

$$\tilde{\phi}_u = \tilde{\phi}_d + 2(\tilde{\phi}_d - \phi_d) \quad (19)$$

with the minmod limiter:

$$\phi_u = \max(0, \min(1, \tilde{\phi}_u)) \quad (20)$$

where the $(\tilde{})$, in the present context, represents a local extrema of the value.

2.4.3 | Petrov-Galerkin and LES stabilisation

To deal with turbulent flow and associated numerical instabilities, an implicit sub-grid scale filtering through a Smagorinsky's model²⁷ is used to discretise the momentum equations. An explicit Large-Eddy Simulation (LES) turbulence model is also implemented within the adaptive meshing approach of the modelling framework; while considering the variability of the adaptive mesh element spatial dimensions, the filter is additionally allowed to vary in space and time. Additionally, in order to add further stabilisation, the Petrov-Galerkin method^{28,29,30} is also applied to the momentum equations, using an upwind weighting of the equations and an additional diffusion term in the direction of the gradient of the solution.

2.4.4 | Hydrostatic force balancing

Following the work by Maddison *et al.*³¹ on the balanced pressure decomposition method formulation and discretisation to unstructured mesh domains, we consider Equations (3) in as a generalised form of forces, and limited to no-normal flow on

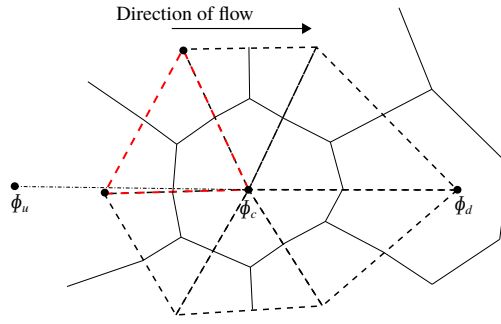


FIGURE 2 Diagram shows the upwind ϕ_u and downwind face ϕ_d values with reference to 2D finite-elements/control-volumes. Here the direction of flow is assumed to be from left to right. The upwind element is highlighted with a red border, ϕ_c is the extrapolated face value of the current element, image modified from¹⁰.

boundary Dirichlet condition, as:

$$\rho \frac{D\mathbf{u}}{Dt} = -\nabla p + \mathbf{b} + \mathbf{F}, \quad (21)$$

subject to $\nabla \cdot \mathbf{u} = 0$, $\mathbf{u} = \mathbf{u}_D$ on $\partial\Omega$, where \mathbf{b} is the buoyancy force, and \mathbf{F} are all the other forces (such as advection and viscous dissipation associated forces, and surface tension), \mathbf{u} is the Eulerian velocity, \mathbf{u}_D is the velocity on the boundary $\partial\Omega$. One can use a Helmholtz decomposition of the momentum Equation (21) to obtain a pressure balance equation, which includes the buoyancy force, \mathbf{b} , and a residual pressure equation which includes ‘all other forces’ term \mathbf{F} .

The inclusion of a hydrostatic pressure solver within the modelling framework allows it to accurately represent a hydrostatic balance, essential for resolving complex flows in a gravitational field. Implementation of force balancing in an adaptive, unstructured meshing framework additionally allows evolving interface topography of multiphase flows, such as slug flows, to be captured in a robust manner.

2.4.5 | Parallel anisotropic mesh optimisation and mesh-to-mesh interpolation

Adaptive mesh optimisation schemes have been shown to significantly reduce the computational overhead of numerical schemes, while retaining accuracy^{20,32,33,34,35}. Optimisation of the mesh is based on libraries first implemented by Pain *et al.*³² which allows mesh alteration using a combination of h (node addition/removal) and r (node re-location) techniques, while retaining external and internal boundaries of the domain. In order to optimise the mesh, the Hessian (a square matrix formed from the partial derivatives) of the field is calculated to determine the local curvature; a high curvature signals the need for local mesh-refinement (e.g. at the interface between phases, the free-surface), while low curvature suggests that the mesh can be coarsened³⁶. First, \mathbf{E} , a metric used for adaptivity computation based on the the Hessian \mathbf{H} is calculated as:

$$\mathbf{E} = \det |\mathbf{H}|^{\frac{-1}{2\gamma+\delta}} \frac{|\mathbf{H}|}{\epsilon} \quad (22)$$

where ϵ is a user-defined weight (the required tolerance for the field introduced by the user), γ indicates the degree of the polynomial of the norm used and δ is the dimension of the space in the problem. The metric provides a value for the quality of the mesh, the bound of the L_2 -norm interpolation error (introduced by the FE representation) with a target value of ϵ . The quality of the mesh can thus be defined as:

$$Q = \sum_{i \in \text{edges}} (\mathbf{e}_i^T \mathbf{E} \mathbf{e}_i - 1)^2 \quad (23)$$

where \mathbf{e}_i define the edges connecting the vertices of the mesh. Mesh anisotropy, mesh gradation level and maximum number of elements are also mesh optimisation parameters to be taken into account if specified by the user. Minimum and maximum triangle or tetrahedral finite-element edge lengths are used to constrain the local resolution of the mesh throughout the simulation. Stability of solutions using large aspect ratio elements to optimise the interface and free-surface in high Reynolds number flows has been recently demonstrated by Via-Estrem *et al.*¹⁵ using the DCV method for discretisation of pressure using control-volumes as in¹⁴ (see Section 2.3).

Conservation of fields between the pre- and post-optimised mesh is ensured using conservative mesh-to-mesh projection between the pre- and post-adapt states of the domain. Generally, a standard consistent interpolation method has been used for projection^{37,38}. However, in this paper, a continuous Galerkin projection method^{39,38} is used for the pressure and component

fraction fields due to its high-order order and mass conservation properties, and for momentum conservation a discontinuous Galerkin projection is used with velocity.

2.4.6 | Metric advection of mesh

To reduce error during the mesh adaptivity process and increase accuracy of the solution, resolution of the mesh is additionally optimised predicting the flow velocity and distance ahead of time. By ensuring that higher resolution of the mesh is present at future times, the ‘metric advection’ method⁴⁰ attempts to reduce the error metric ahead of time and flow. As an example, if the interface is moving with velocity \mathbf{u} , then according to the metric advection CFL requirement imposed on the system C^M , the metric advection routine will increase resolution ahead of the interface such that the error between the predicted ‘future’ CFL number ($\Delta t |\mathbf{u} \cdot \mathbf{n}| / h_{d_1 d_2} = C^f$) is equal to C^M ahead of the flow, where $h_{d_1 d_2}$ is the distance between centroids of the downwind control-volume (d_1) and next downwind control-volume (d_2) normal to the flow.

3 | NUMERICAL BENCHMARKING AND EXAMPLES

3.1 | Rayleigh-Taylor Instability

The modelling framework of this paper is used to simulate a moving interface problem with complex topological changes, the Rayleigh-Taylor instability problem, to validate the accuracy of the scheme and evaluate the robustness of the integration of methods described in this paper. In the Rayleigh-Taylor instability problem, two immiscible fluids of different densities are separated, in a gravitational field, with an initial perturbation in the interface, leading to a free-surface instability where the higher dense fluid pushes into the lower dense fluid^{41,42}. It is generally known that several stages of development which can be categorised when observing the Rayleigh-Taylor instability problem^{43,42}: (1) an initial growth stage, where the amplitude of the perturbation grows exponentially with time; (2) a terminal velocity growth stage, where the amplitude of the perturbation grows non-linearly with the heavy fluid (referred to as the ‘spike’) while penetrating the light fluid (referred to as ‘bubble’); (3) re-acceleration of growth stage driven by Kelvin-Helmholtz instability resulting in development of structures along the spike; (4) a turbulent or chaotic development stage which can lead to break-up of the spike structure. In this section, we compare the simulation results from two- and three-dimensional Rayleigh-Taylor instability problems against previous numerical studies^{44,45,46,47}. We additionally make comparisons against experimental investigation by Waddel *et al.*⁴⁸.

3.1.1 | Problem set up and mesh-generation

To set up a numerical investigation of the Rayleigh-Taylor instability problem, two immiscible fluids are separated by an interface as shown in Figure 3. The heavy fluid is situated above a lighter fluid with an initial ‘single-instability’ sinusoidal perturbation (following the work of Tryggvanson *et al.*^{44,45}) in the interface initialised along the vertical axis with the form:

$$y(x) = h + \varepsilon \cos(2\pi x) \quad (24)$$

where y measures distance from the bottom of the computational domain, $h = 1.86D$ is the initial mean position of the interface, D is the width of the computational box (internal pipe diameter), x is the distance along the horizontal axis, and ε is the amplitude of the perturbation set to $0.1D$. No-slip and free-slip boundary conditions are imposed as shown in Figure 3 for a domain $0 \leq x \leq 1$ and $0 \leq y \leq 3$. We set the density ratio $\rho_1/\rho_2 = 3$, and the viscosity ratio $\mu_1/\mu_2 = 9.81$, where ρ_1 and μ_1 , and ρ_2 and μ_2 represent the density and viscosity of the heavier and lighter fluids, respectively. We also set the Reynolds number to $Re = \rho_1 D^{2/3} g^{1/2} / \mu_1 = 3000$, and the Atwood number to $A = (\rho_1 - \rho_2) / (\rho_1 + \rho_2) = 0.5$; these are the same parameters used in^{44,45,46,47}. Time and velocity are scaled on $t = \sqrt{D/Ag}$ and $u = \sqrt{AgD}$, respectively. Several surface tension coefficients σ (which can also be non-dimensionalised to the Weber number $w = \rho Ag D^2 / \sigma$) were also compared, starting from 2×10^{-1} N/m to 2×10^{-4} N/m, for the two-dimensional validation study.

Two-dimensional (2D) and three-dimensional (3D) numerical validation studies were carried out using both fixed and adaptive meshes. Fixed, structured meshes were generated in GMSH⁴⁹: a coarse mesh with 50×150 elements (see Figure 4a) and a fine mesh with 100×300 elements (see Figure 4b). Starting from the initial structured meshes, two further simulations were run with adaptive mesh optimisation. The meshes after the initial adaptive step are shown in Figures 4c and Figure 4d), where it can be seen that the interface is clearly captured with a specified minimum and maximum element edge lengths (e^{min} and e^{max} , respectively) used for adaptive mesh optimisation. Adaptive time-stepping was employed with a constraint based on CFL= 1 The

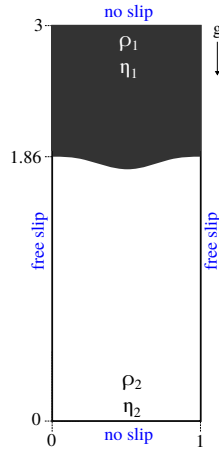


FIGURE 3 Initial setup for the Rayleigh-Taylor instability problem illustrating the (a) 2D geometry and material properties, with the boundary conditions in blue.

calculation is carried out with $P1_{DG}-P1_{CV}$ (denoting linear piece-wise Discontinuous-Galerkin linear piece-wise Continuous-Galerkin) velocity-pressure element pair. Secondly, three-dimensional (3D) simulations were conducted with a fixed, structured mesh similar to that in Figure 4b but in a cylindrical domain with dimensionless radius of 1 as in the initial setup. The 3D adaptive mesh simulation was initialised with a structured mesh using an initial adaptive mesh optimisation stage, as in the 2D setup. The resultant ‘optimised’ mesh is shown in Figure 4e and Figure 4f as the whole mesh and domain slice, respectively.

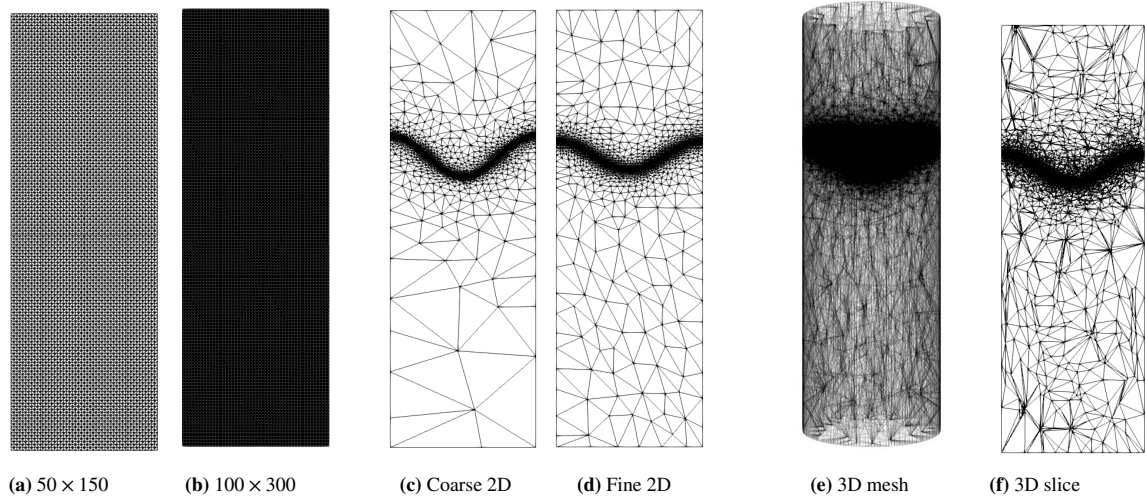


FIGURE 4 Optimisation of mesh-generation. Coarse and fine fixed grids of 30,000 triangles and 60,000 triangles, (a) and (b), respectively; coarse ($e^{min}, e^{max} = \frac{1}{1000}, \frac{1}{2}$) and fine ($e^{min}, e^{max} = \frac{1}{1000}, \frac{1}{5}$) adaptive meshes comprising 10,000 and 15,000 elements, (c) and (d), respectively; the initial time-step adapted mesh ($e^{min}, e^{max} = \frac{1}{1000}, \frac{1}{5}$) for the 3D simulation is shown in (e) and the associated unstructured mesh on a cut-plane normal to the page is presented in (f).

3.1.2 | Two-dimensional simulation results

In this section, we verify the implementation of the full integrated modelling framework by comparing the evolving features of the Rayleigh-Taylor instability problem, characterised by a penetrating spike and rising bubble of a high and lower dense liquid (see Figure 5 for reference), respectively in 2D. We make comparisons between the fixed mesh results (using the mesh

as in Figure 4b) and adaptive mesh results (using the mesh as in Figure 4c), including benchmarking computational efficiency between the two cases.

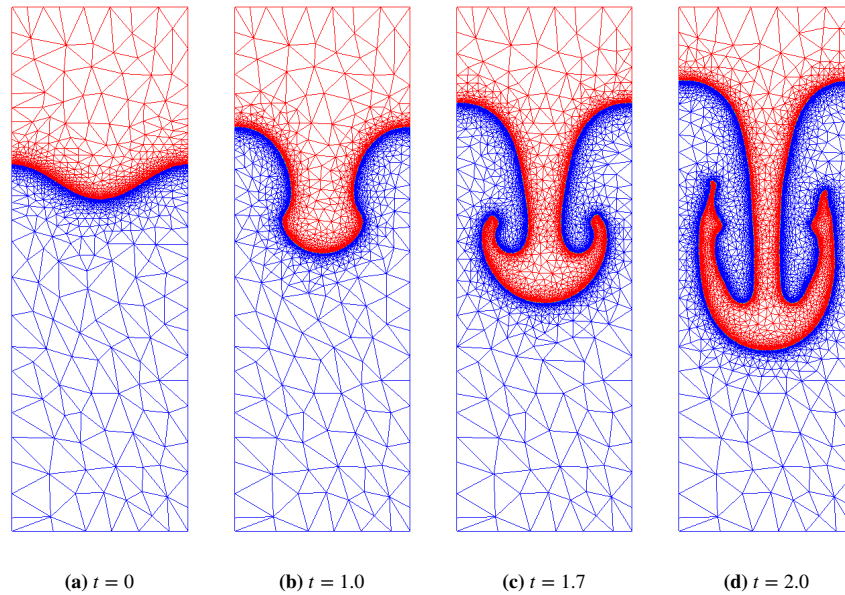


FIGURE 5 Interface shape and mesh for four time levels of the higher and lower dense fluids showing the spike (the heavier fluid) and bubble (the lighter fluid), coloured red and blue, respectively, with surface tension coefficient of 0.02 N/m ($w = 7.4 \times 10^2$) and $A=0.5$

Simulations were run using the fixed meshes shown in Figures 4a-4b as initial meshes. For the fixed, structured mesh simulations, adaptive mesh optimisation was not used, so these meshes remain unchanged throughout the computations. For the adaptive mesh simulations, adaptive mesh optimisation was used throughout (including to generate the initial unstructured mesh (Figures 4c-4d) from the starting fine resolution structured mesh in Figure 4b). It can be seen that the modelling framework with adaptive mesh optimisation (see Figure 5) can effectively capture the rapidly varying interfacial structure. When measuring the growth rates of the bubble and spike fronts, very good agreement is found between the integrated framework results of fixed and adaptive meshes and the numerical experiments available in the literature^{45,46,47} in Figure 6. It is possible that discrepancies in the correlation of latter time growth rates might be a result of differences in resolving the dynamics of chaotic turbulent development stage in the numerical experiments. Importantly, the total number of element (and degrees of freedom) associated with the adaptive mesh results is significantly lower than that required for the fixed mesh simulation throughout the computation (see Figure 7a). The computational time is also considerably less as shown in Figure 7b highlighting the improvement in computational efficiency with adaptive mesh optimisation.

Direct comparisons of the spike and bubble features of the Rayleigh-Taylor problem against experimental laboratory results, obtained using Planar Laser-Induced Fluorescence (PLIF), by Waddell *et al.*⁴⁸, are shown in Figure 8. The comparisons shows very close resemblance between the shape and profile of the spike and bubble of the numerical results and experimentally-imaged results of Waddell *et al.*⁴⁸. Waddell *et al.* made the observation that surface-tension effects “should only have substantial effect at the smallest observed scales”, which can be seen when varying surface tension as in Figure 9. Closer observation of the evolving bubble feature, and comparisons to the numerical results, for two different surface tension coefficients are visualised in Figure 9. Here, it can be seen that the numerical results, especially of the lower surface tension, closely resemble the observed profile of the evolving bubble by Waddell *et al.*⁴⁸ at the smaller scale features.

We benchmark the integration of interface capturing and force-balancing alongside adaptive mesh optimisation in the modelling framework by observing the evolution of the feature of the bubble and spike, and comparing to literature. Initially comparing numerical results with and without interface capturing and force-balancing, in Figure 10 we can see noticeable deviation in the latter time position of the bubble (see Figure 10a) and spike (see Figure 10b) when comparing with the full integrated method presented in this paper, and the results of^{45,46,47}. Including interface capturing, but no integration of force-balancing we

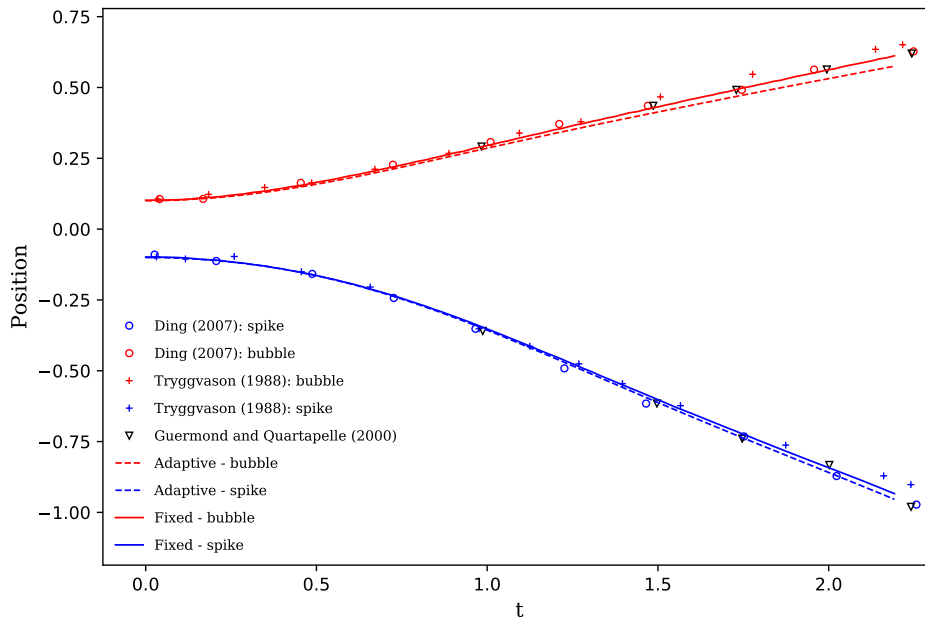


FIGURE 6 Position of penetrating spike tip (blue) and rising bubble tip (red) versus time for the Rayleigh-Taylor instability simulation compared with numerical experiments reported in literature

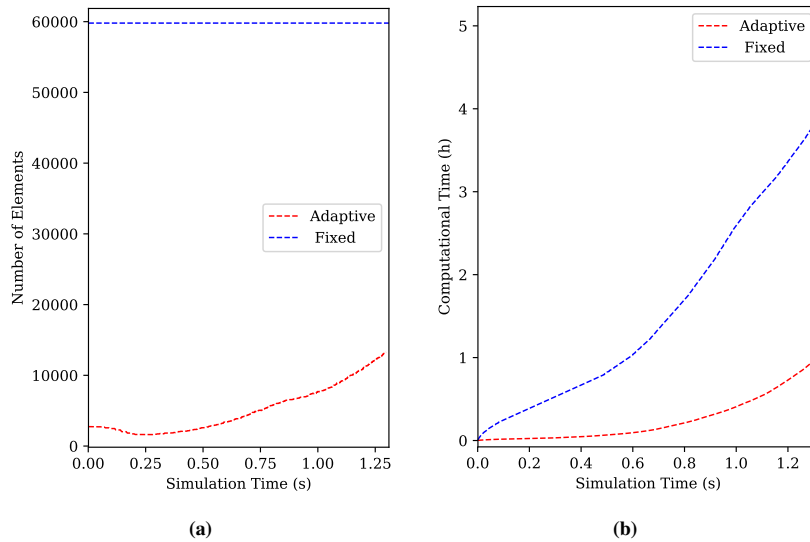


FIGURE 7 Comparison of total number of elements (a) and computational time (b) between adaptive (red) and fixed (blue) mesh simulations with equivalent minimum element edge-length resolution e^{min} of 0.01

can see that there is also noticeable difference in the position of the penetrating spike with no force-balancing of surface tension and hydrostatic forces (see Figure 11).

When comparing numerical results for the surface tension values of 0.0002 N/m and 0.02 N/m ($w = 7.4 \times 10^4$ and 7.4×10^2 , respectively), significant variation in the formation of instabilities and break-up structures at the spike-bubble interface is observed (see Figure 12), more evident during latter stage development of the instability. Integration of adaptive mesh optimisation alongside the force-balancing, the grid is well optimised to well resolve the resulting structural variations of the interface

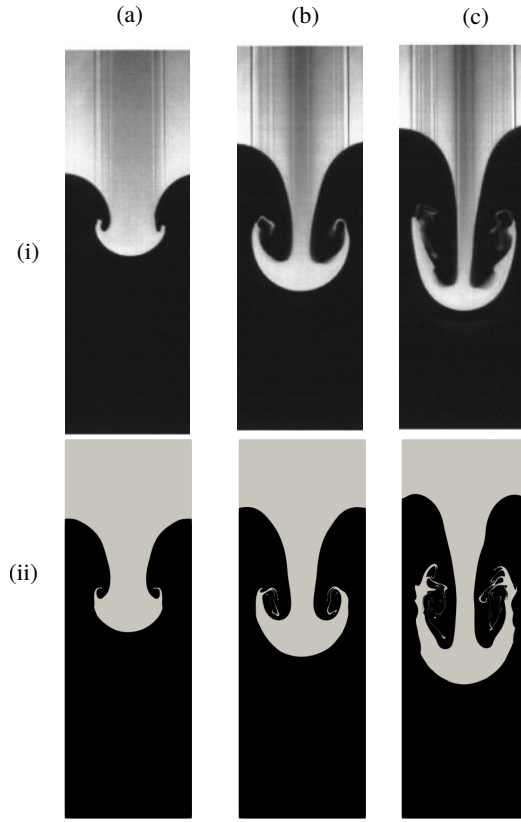


FIGURE 8 Direct comparisons of bubble and spike experimental PLIF results from the work of Waddell *et al.*⁴⁸ for (i) vs our numerical results with $A = 0.334$ and $a = 1.34g$ (ii), and surface tension coefficient of 2×10^{-4} N/m ($w = 4.4 \times 10^4$). Total simulation time was $t = 2$.

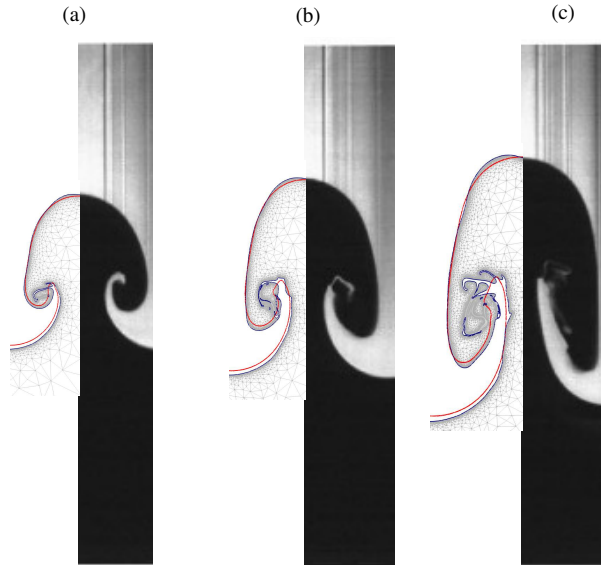


FIGURE 9 Direct comparison of bubble experimental results PLIF from⁴⁸ for (right) experimental results of $A = 0.334$ and $a = 1.34g$ vs (left) numerical results of $A = 0.334$ for three different times and two different surface tension coefficients of (red) 2×10^{-2} N/m and (blue) 2×10^{-4} N/m ($w = 4.4 \times 10^4$ and 4.4×10^2 , respectively). Total simulation time was $t = 2$.

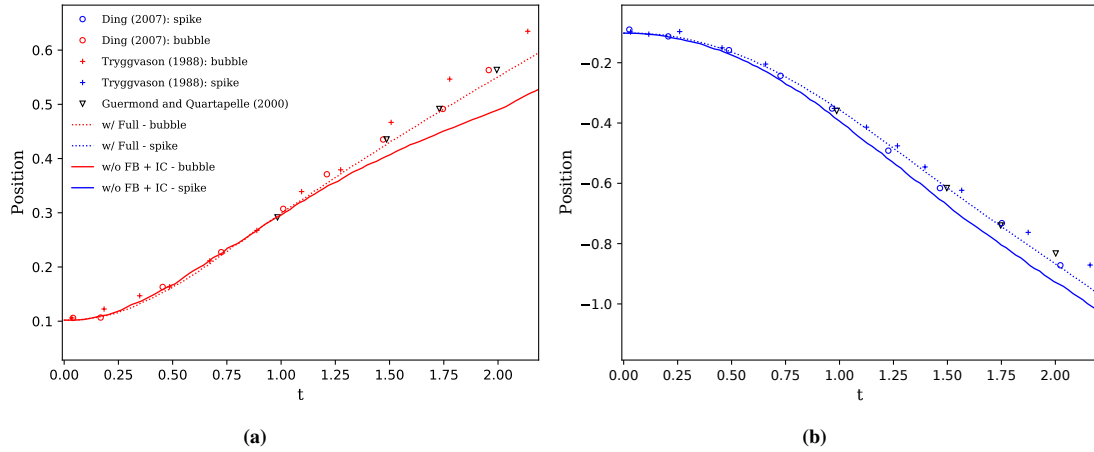


FIGURE 10 Position of penetrating spike tip (blue) and rising bubble tip (red) versus time for the Rayleigh-Taylor instability simulation comparing numerical simulations for the full integrated (dotted) and non integrated framework (unbroken). Here ‘Full’, ‘FB’ and ‘IC’ denote the full modelling framework with (force-balancing and interface capturing), no interface capturing and with only interface capturing, respectively

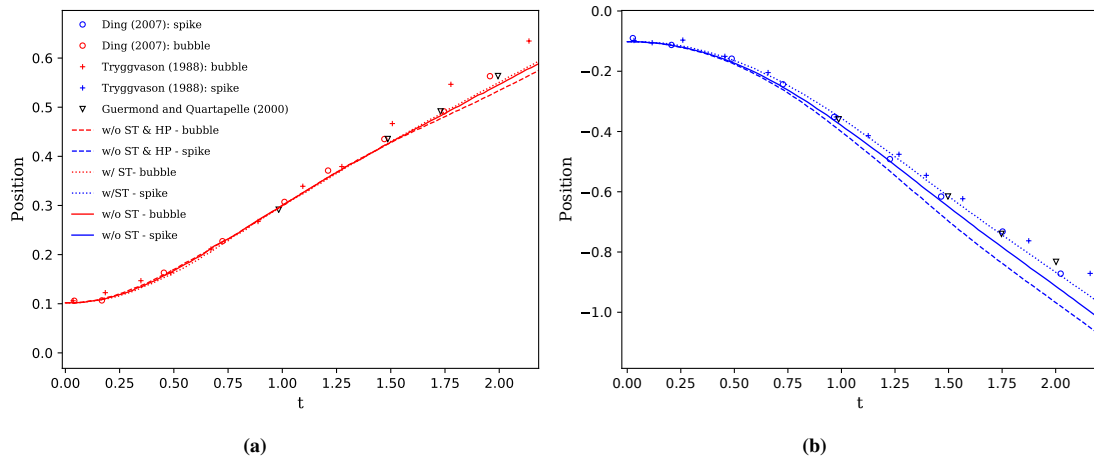


FIGURE 11 Position of penetrating spike (blue) tip and rising bubble tip (red) versus time for the Rayleigh-Taylor instability simulation comparing numerical simulations with and without force-balancing of surface tension and hydrostatic forces (dotted line), and without only surface tension (unbroken line). Here ‘ST’ and ‘HP’ denote surface tension and hydrostatic pressure force-balancing, respectively

during the evolution of the spike and bubble. This especially evident in cases with lower surface tension as in Figure 12a-c, compared to higher surface tension (see Figure 12d-f) where ligament formation and Kelvin-Helmholtz instability at the interface is less prominent.

3.1.3 | Three-dimensional simulation results

Numerical three-dimensional validation of the Rayleigh-Taylor instability problem were carried out using a cylindrical domain of internal diameter D and height L . The modelling parameters were consistent with the same regime as the two-dimensional validation study ($Re = 3000$, $A = 0.5$ and gravitational acceleration $1g$) and reported literature used for the benchmarking

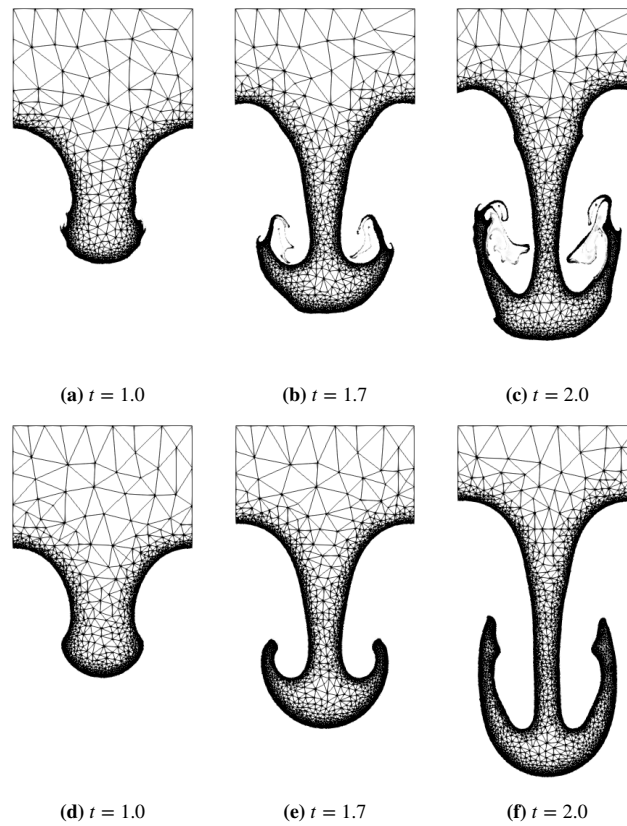


FIGURE 12 Interface profile and mesh for three time levels comparing two different surface tension coefficients of 0.0002 in (a)-(c) and 0.02 in (d)-(f) ($w = 7.4 \times 10^4$ and 7.4×10^2 , respectively)

study^{45,46,47}. The initial mesh used for the simulation is a GMSH generated partially structured mesh of 2.5M tetrahedral elements with a $0.02L$ element edge length. This mesh was also used as the input mesh to generate the initial mesh, optimised on the interface as in the 2D adaptive mesh simulations, for the comparative simulation with adaptive mesh optimisation. Two scenarios are presented for the 3D numerical study. Firstly, using the integrated modelling presented in this paper, a preliminary fixed mesh simulation of the single-perturbation Rayleigh-Taylor instability is conducted without adaptive mesh optimisation. Next, the full modelling framework with adaptive mesh optimisation is used to model the same problem to compare the capability of the full framework. The 3D simulations were computed in parallel on a high-performance computing multi-node cluster using Intel Ivy-Bridge CPUs with up to 140 cores.

From initial observations of the Rayleigh-Taylor instability using a fixed unstructured mesh, shown in Figure 13, it is clear that the force-balancing and adaptive meshing in the integrated modelling framework captures the characteristic evolution of the penetrating spike and rising bubble of the lower density fluid under gravity. The initial growth stage, and subsequent stages, including the development of structures along the spike and start of the chaotic break-up of the spike is evident in the results shown in Figure 13.

Applying the full integrated modelling approach detailed in this paper (with adaptive mesh optimisation), results of three-dimensional Rayleigh-Taylor instability problem using adaptive mesh optimisation are presented in Figure 14. It is clear from initial observations that the characteristic behaviour of the single-perturbation Rayleigh-Taylor instability problem and development stages are well captured with the integrated framework and adaptive mesh optimisation. From Figure 15 showing the corresponding slice of the 3D adaptive mesh, it can be seen the spike and bubble profile closely resemble the 2D results, including the formation of ligaments near the interface at latter simulation times (due to chaotic break-up of the spike). However, some noticeable differences can be identified upon comparing the 2D and 3D numerical results as a result of 3D effects captured by the integrated modelling framework: (i) element-scale mesh heterogeneity introduced by initial interface perturbation function coinciding with the generated initial unstructured tetrahedral mesh leads to small-scale instabilities that develop into secondary

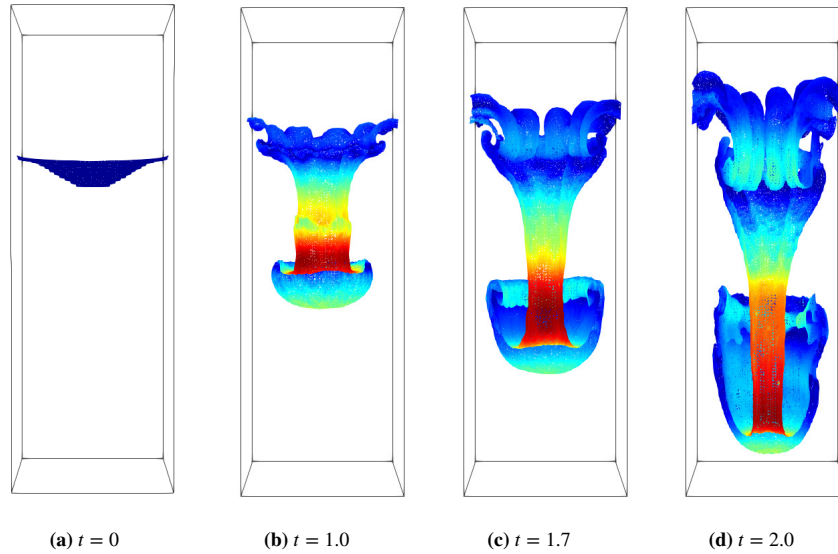


FIGURE 13 Clip taken at the centre plane of the mesh wire-frame rendering (of the high-density fluid) for four time-steps of 3D numerical results using coarse fixed mesh with 2.5M tetrahedral elements with a $0.02L$ element edge length, visualised using velocity magnitude for the colour scheme. Here, as with the 2D study, $Re = 3000$, $A = 0.5$ and gravitational acceleration $1g$.

structures in the bubble front. This is more pronounced at the latter stages of evolution, when the height of the bubble front significantly varies asymmetrically along the cylinder walls; (ii) presence of latter-stage two-layer roll-up of the interface as a result of 3D effects during Rayleigh-Taylor instability development^{42,50}; (iii) asymmetrical formation of ligaments and Kelvin-Helmholtz instabilities in close proximity to the spike-bubble interface are evident in the 3D results (as seen in Figure 15), captured by adaptive optimisation (refinement) of the grid near the interface.

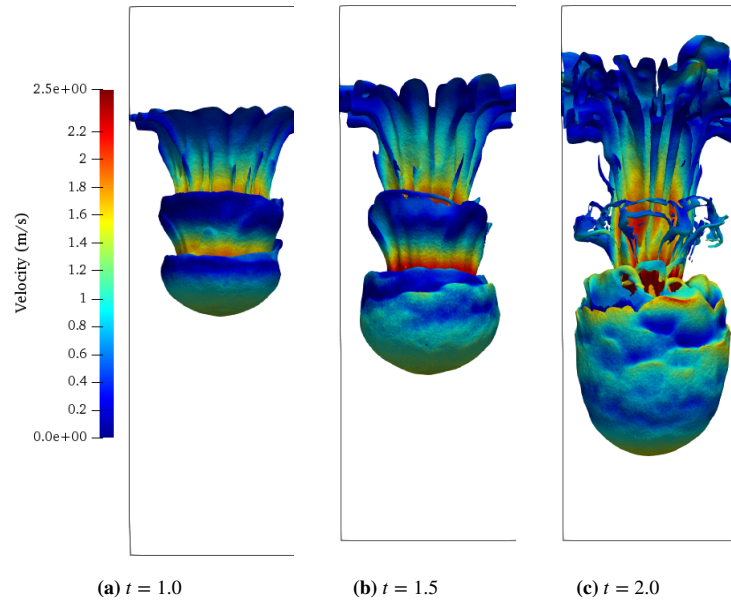


FIGURE 14 Interface contour volumetric rendering (with velocity colour) of high-density fluid at different non-dimensional time values showing the formation of ligaments and Kelvin-Helmholtz instability of the surface.

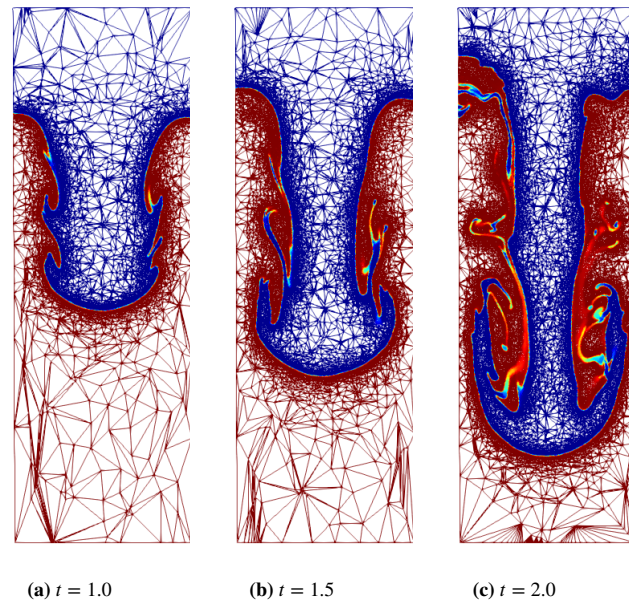


FIGURE 15 2D slice (zx-plane) of the adaptive volumetric mesh showing the mesh at different times, with low-density and high-density phase volume fractions as red and blue, respectively for $A=0.5$.

3.2 | Free-Bubbling Flow

Free-bubbling flow in high-aspect ratio domains encompasses strong coupling of mechanisms (e.g. surface driven flows and buoyancy) that can be a challenging evaluation problem requiring the full range of methods and technologies integrated in the modelling framework. In this section, we evaluate the integrated framework for modelling complex flow patterns, with interface capturing and force-balancing using a three-dimensional numerical simulations of multi-fluid injection into a long pipe is presented in both the laminar and turbulent flow regimes.

3.2.1 | Laminar Flow Regime

The results of free-bubbling flow are presented from numerical simulations based on experiments by Mayor *et al.* in¹ for vertical slug flow in the laminar regime. In the simulation, air is injected through a hole of diameter d into a vertical pipe (of length L and outer pipe diameter D) filled with a liquid Glycerol solution (see Figure 16). The parameters used in this numerical study are presented in Table 2. The calculation is carried out with $P1_{DG}-P1_{CV}$ velocity-pressure element pair, and adaptive meshing with minimum and maximum element edge lengths of 1×10^{-3} m and 2.5×10^{-1} m, respectively.

Figure 17 shows snapshots of the modelling domain visualising the air phase at early simulation times, during the generation, pinching, and detachment of an air bubble close to the air-inlet. Snapshots of the modelling domain visualising contours of the gas phase at early simulation times can be seen in Figure 18, including close-up snapshots of the adaptive mesh during initial bubble generation. It can be seen that the resolution of the adaptive mesh around the air-liquid is well refined by mesh adaptivity to capture the rising bubble topography, whereas in other regions requiring lower resolution, the elements are significantly coarser, thus reducing the overall computational overhead burden of the mesh (as opposed to an equivalent fixed resolution mesh).

Figure 19 shows snapshots of free-bubbling flow latter development stages, including multiple bubble generation and coalescence, and sustained rise due to buoyancy. The bubbles generated at the inlet stream of air gains regularity in the bubble spacing (the distance between consequent bubbles) and shape, deforming to a ‘bullet-shaped’ profile as the bubbles propagate up the length of the vertical pipe (see Figure 19c). The shape and profile of the bubble shapes are also observed in the experimental work of Mayor *et al.*¹ which this numerical example is based on.

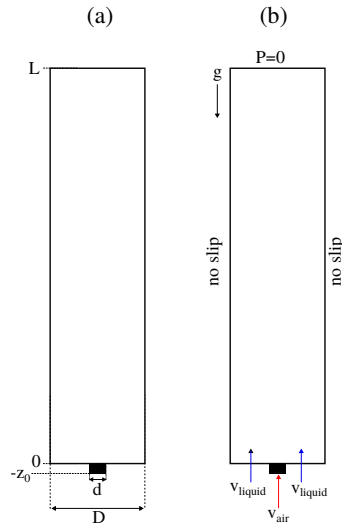


FIGURE 16 Initial setup for the free-bubbling flow problem illustrating the (a) geometrical dimensions, and (b) the boundary conditions.

TABLE 2 Computational parameters for the glycerol-air vertical slug flow.

Parameter	Value	Unit
Surface tension	0.64	N/m
Pipe length	$200 \cdot D$	m
Gravitational acceleration	9.81	$\text{m} \cdot \text{s}^{-2}$
LIQUID (GLYCEROL)		
Viscosity	0.114	$\text{kg} \cdot (\text{m} \cdot \text{s})^{-1}$
Density	1.1×10^3	$\text{kg} \cdot \text{m}^{-3}$
Superficial velocity v_l	0.21	$\text{m} \cdot \text{s}^{-1}$
Inlet diameter (D)	0.032	m
GAS (AIR)		
Viscosity	1.81×10^{-5}	$\text{N} \cdot \text{m} \cdot \text{s}^{-1}$
Density	1.125	$\text{kg} \cdot \text{m}^{-3}$
Superficial velocity v_a	0.38	$\text{m} \cdot \text{s}^{-1}$
Inlet diameter (d)	0.003	m

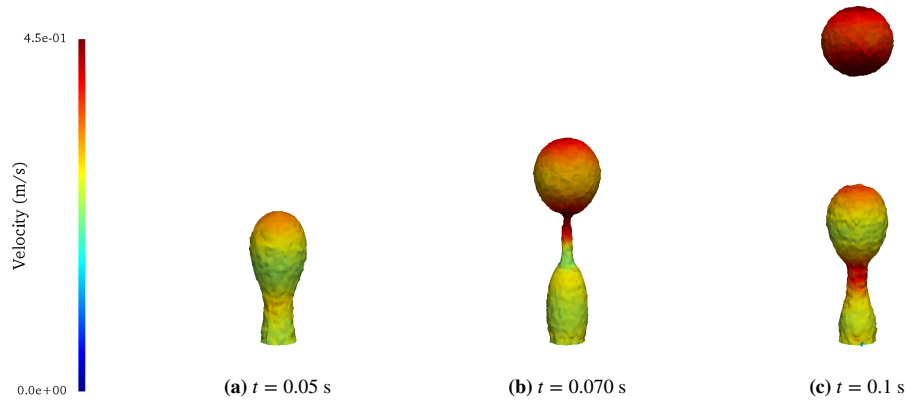


FIGURE 17 Zoomed snapshots of initial bubble (a) emergence, (b) formation and (c) detachment stages of laminar vertical slug flow with v_a and v_l of 0.38 ms^{-1} and 0.21 ms^{-1} , respectively

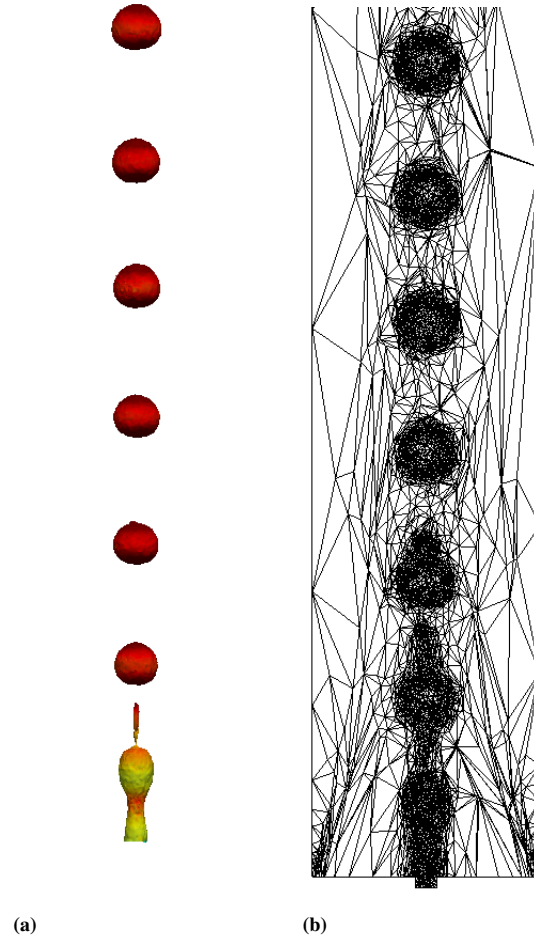


FIGURE 18 Snapshots of different aspects of developing flow pattern at $t = 3.0\text{s}$ showing (a) Focused region at the inlet visualising contours of air-liquid interface volumetric contours (velocity colouring), and (c) visualising a slice of the mesh wire-frame of the focused region at the inlet of the domain

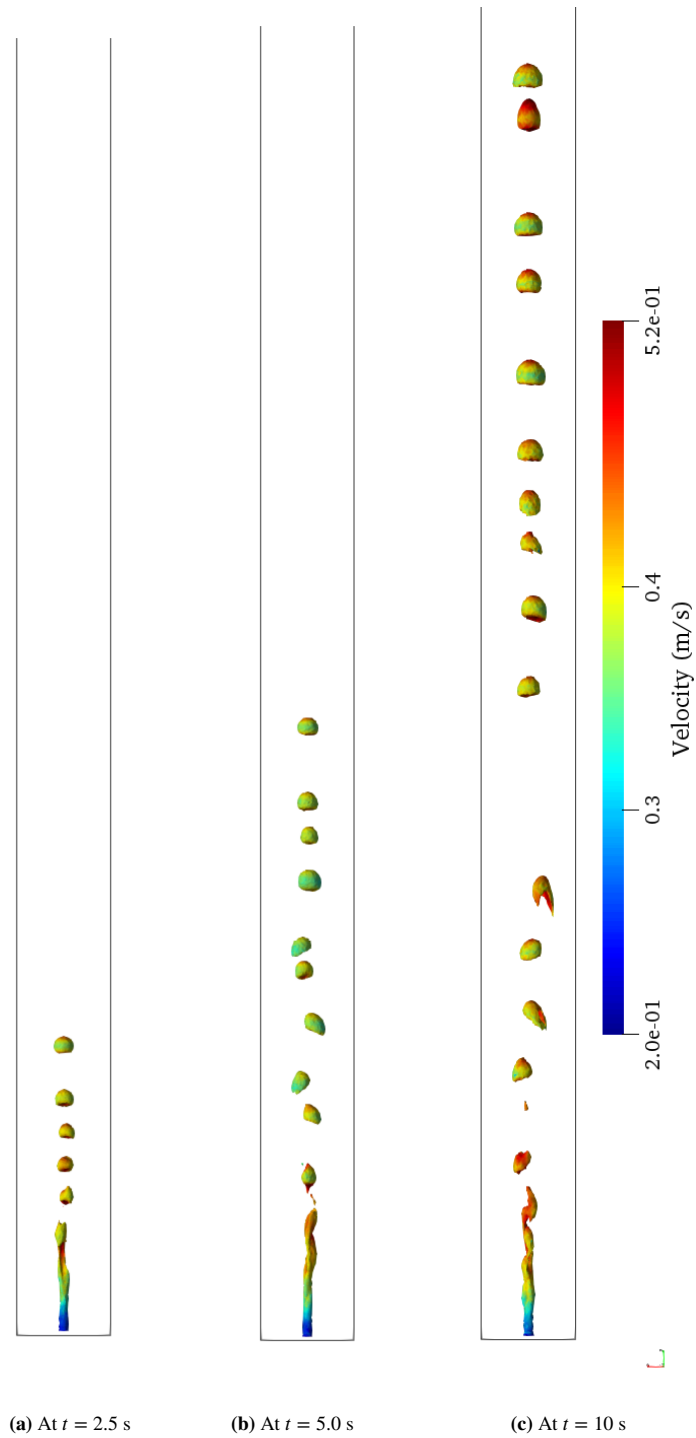


FIGURE 19 Snapshots of three-different simulation times visualising flow pattern as contours of the air-liquid interface with velocity magnitude colouring.

3.2.2 | Turbulent Flow Regime

The modelling framework has been applied to investigate vertical pipe slug flow in the turbulent regime based on experimental investigation by Mayor *et al.* in⁵¹. Similar to the previous laminar regime investigation, in this simulation, air is injected through a hole of diameter d into a vertical pipe (of length L and outer diameter of D) filled with water. The computational parameters used in this numerical study are presented in Table 3. The calculation is carried out with P1_{DG}P1_{CV} element pair, and adaptive meshing with minimum and maximum element edge lengths of 1×10^{-3} m and 2.5×10^{-1} m, respectively.

TABLE 3 Computational parameters for the water-air vertical slug flow.

Parameter	Value	Unit
Surface tension	0.72	N/m
Pipe length	200·D	m
Gravitational acceleration	9.81	m·s ⁻²
LIQUID (WATER)		
Viscosity	1×10^{-3}	kg·(m·s) ⁻¹
Density	1×10^3	kg·m ⁻³
Superficial velocity v_l	0.21	m·s ⁻¹
Inlet diameter (D)	0.032	m
GAS (AIR)		
Viscosity	1.81×10^{-5}	N·m s ^{-s}
Density	1.125	kg·m ⁻³
Superficial velocity v_a	0.38	m·s ⁻¹
Inlet diameter (d)	0.003	m

Figure 20 shows snapshots of the modelling domain visualising the air phase at early simulation times and focused on the region close to the air-inlet showing generation, pinching and detachment of the bubble. Formation to total detachment of the initial air bubble is first observed to initiate at 0.18 seconds to 0.22 seconds after start of injection of air into the modelling domain. Subsequent detachment events are seen every 0.2 seconds in the simulation after the initial generation of the air bubble. Figure 21 shows snapshots of the developing flow pattern, visualising consecutive multiple bubble generation and detachment from the free-flowing air inlet.

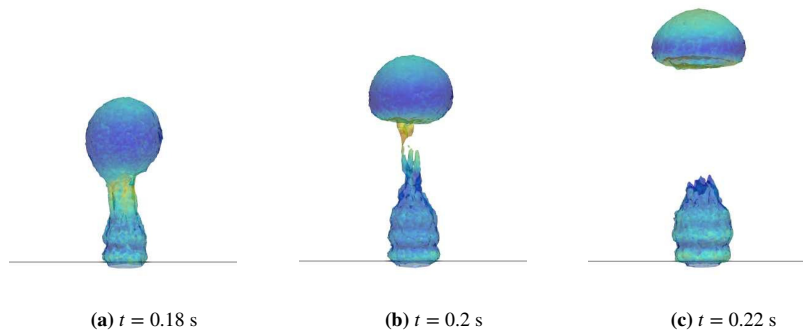


FIGURE 20 Zoomed snapshots of initial turbulent bubble flow (a) emergence, (b) formation and (c) detachment stages of the simulation.

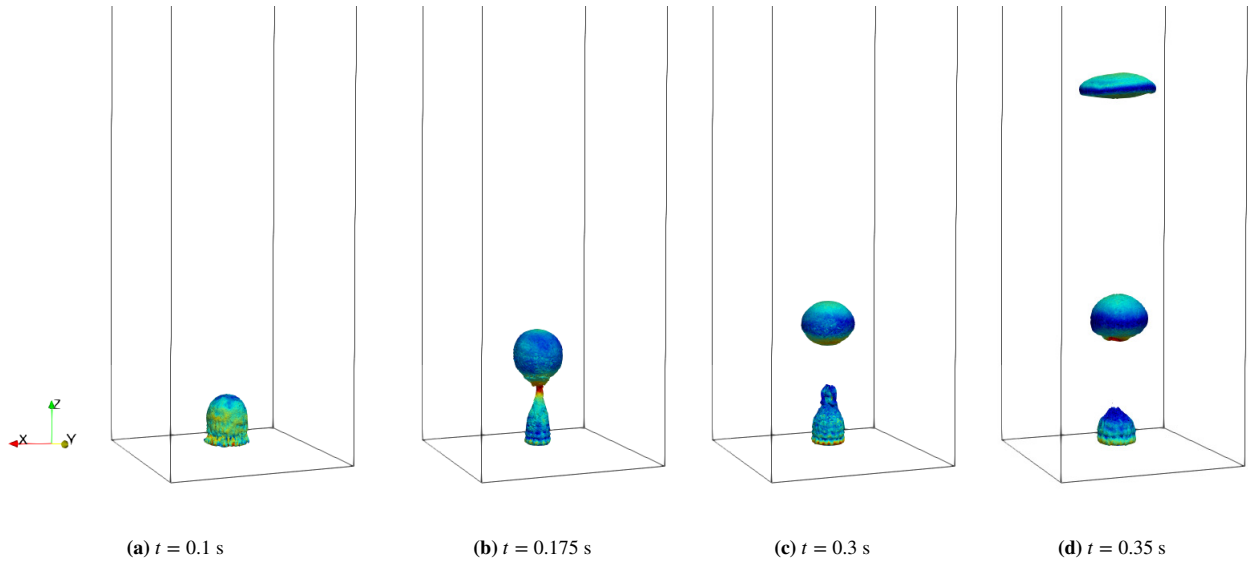


FIGURE 21 Snapshots of four different simulation stages showing contours of free-bubbling air phase in a vertical pipe, zoomed into the initial bubble generation region.

4 | DISCUSSION

Modelling turbulent multiphase flow dynamics in pipes and pipe networks present a two-fold challenge: (1) resolving important mechanisms (such as Helmholtz instabilities) leading to complex flow patterns, and (2) capturing the complex transient flow in realistic modelling domains while maximising computational efficiency. The methods presented in this paper (Section 2) are integrated into the existing multi-component modelling code IC-FERST-Fluidity to give a complete parallel framework to accurately model complex multiphase flow in realistic scenarios, such as in pipes and pipe networks. The main methods in the framework that are integral to achieving this are: (i) compressive advection scheme to ensure interface between phases are kept sharp, (ii) spatial optimisation of the mesh using highly anisotropic mesh optimisation, (iii) combined finite-element and control-volume methods for stability of ‘poor elements’, (iv) hydrostatic pressure solver for robustly resolving force balances in a gravitational field, and (v) surface tension for resolving complex interfacial behaviour with coarse mesh resolutions and poor quality elements.

Section 3 clearly shows validation and benchmarking of the DCV multi-component method modelling framework highlighted in this paper. Using the methods summarised in Table 1, the dynamics of Rayleigh-Taylor instability problem are well captured in 2D and 3D, detailed in Section 3.1.2 and Section 3.1.3, respectively. Both quantitative comparisons with literature, and qualitative comparisons with experiment PLIF results show very good agreement with literature. Anisotropic adaptive mesh optimisation with interface capturing is used to significantly improve resolution around the interface while ensuring that total computational overhead due to the mesh size is reduced. Additionally, changes in interfacial tension, captured by the surface tension force balance model, play a significant role in determining the occurrence ligament formation and Helmholtz instability on the interface. Similar to observations reported by^{42,50}, two-layer roll-up phenomena is observed for the heavier fluid, which is not observed in the 2D numerical experiments. Comparing computational efficiency for fixed mesh and adaptive mesh, for the 2D Rayleigh-Taylor study, the efficiency gained by adaptive mesh optimisation represents a significant reduction in total number of elements as the fixed mesh, and a reduction of computational time, for equivalent resolution at the interface. As observed in these numerical experiments, (and similarly noted by Andreas *et al.*⁵² for porous media flow), adaptive mesh optimisation was able to retain high accuracy while significantly reducing the computational cost of the simulation compared to equivalent fixed mesh study.

Section 3.2.1 and Section 3.2.2 demonstrates the numerical framework being used to model and resolve complex multiphase flow transients in the case of free-bubbling flow in both the laminar and turbulent regime, including formation of slug flow in vertical pipes, defined by Taylor bubbles of air separating regions of higher velocity liquid slugs. The characteristic ‘bullet’

shape of the Taylor bubbles generated in the vertical pipe also shows agreement with the observations by Mayor *et al.*^{1,51} of slug flow for the specific superficial velocities. The final investigation establishes the importance of using anisotropic, unstructured adaptive mesh optimisation to resolve the complex topography of the flow transients (such as the shape and size of the Taylor bubbles) and modelling domain (high aspect ratio pipes network), in conjunction with proper force balancing to capture the physics that govern the evolving flow-pattern of multiphase flow.

Detailed quantitative comparisons of complex flow patterns, such as horizontal slug flow and annular flow, in other pipe configurations (such as subsea risers and flexible pipes), are being investigated and will be reported in future work. Furthermore, efforts are directed towards improving parallel scalability and efficiency of the modelling framework to massively parallel computations (2000+ cores) with unstructured, anisotropic mesh optimisation, in large high-performance clusters.

5 | CONCLUSIONS

This paper presents an integrated, parallel, three-dimensional modelling framework for accurate prediction of inertial and turbulent flow dynamics. Using a mixed finite-element and ‘double-control-volume’ discretisation method alongside anisotropic adaptive mesh optimisation, the modelling framework is demonstrated to accurately resolve complex multiphase flow regimes and transients observed in unstable interface applications in pipe flows. The integrated approach includes combination of an extended interface capturing model based on compressive advection method, with surface tension and hydrostatic force solvers, as well as adaptive-implicit time-stepping.

The aforementioned modelling framework was evaluated using the Rayleigh-Taylor Instability problem in two and three dimensions. Benchmarking and validation from an investigation of the single interface instability problem establishes that the framework accurately captures the complex flows and free-surface behaviour that arise in a wide range of applications and flow regimes. Using combined finite-element and control-volume methods, alongside anisotropic mesh optimisation, enabled resolution of the mesh to be concentrated in relatively important regions of the modelling domain, such as the unstable interface, while improving computational efficiency. Additionally, using domain decomposition methods and MPI for parallelisation, the modelling framework presented here has the potential to be used for complex domain geometries with highly complex flow regimes such as free-bubbling flow in large pipe networks. The framework was then used for a preliminary study of free-bubbling slug flow from gas and liquid injection into a vertical column. The investigation looked at complex flow patterns in the laminar and turbulent regimes, with the initial results showing good agreement with experimental observations from the literature. The benchmarking and illustrative results especially demonstrate the high level of detail, and agreement with observations, captured by resolving sharp interfaces using anisotropic unstructured adaptive mesh optimisation and interface capturing. Although horizontal slug-flow and slug-flow formation was not studied in this work, the modelling approach is well suited to simulate complex flow regimes in high-aspect ratio domains and is planned for future work. The integrated modelling approach emphasises the importance of including rigorous force-balancing to provide accurate solutions of complex multiphase flow patterns, while maximising computational efficiency through mesh optimisation and parallelisation for practical realisation.

ACKNOWLEDGEMENTS

The authors gratefully acknowledge the EPSRC project MUFFINS (EP/P033180/1, EP/P033148/1), FAMOS (NE/P017452/1) and programme grant PREMIERE (EP/T000414/1). The ICAM62 framework collaboration with BP plc is also acknowledged. For further information, please contact the corresponding author Asiri Obeysekara at (a.obeysekara@imperial.ac.uk) or the AMCG Group (www.imperial.ac.uk/earth-science/research/research-groups/amcg).

References

1. Mayor T. S., Pinto A. M. F. R., Campos J. B. L. M.. Hydrodynamics of Gas-Liquid Slug Flow along Vertical Pipes in the Laminar Regime: Experimental and Simulation Study. *Industrial & Engineering Chemistry Research*. 2007;46(11):3794-3809.

2. Pavlidis Dimitrios, Xie Zhihua, Percival James R, Gomes Jefferson L M A, Pain Christopher C, Matar Omar K. Two- and three-phase horizontal slug flow simulations using an interface-capturing compositional approach. *International Journal of Multiphase Flow*. 2014;67:85–91.
3. Fabre J. *Advancements in Two-Phase Slug Flow Modeling*. 1994.
4. Fabre J, Line A. Modeling of Two-Phase Slug Flow. *Annual Review of Fluid Mechanics*. 1992;24(1):21–46.
5. King M J S, Hale C P, Lawrence C J, Hewitt G F. Characteristics of flowrate transients in slug flow. *International Journal of Multiphase Flow*. 1998;24(5):825–854.
6. Omebere-Iyari N K, Azzopardi B J, Ladam Y. Two-phase flow patterns in large diameter vertical pipes at high pressures. *AIChE Journal*. 2007;53(10):2493–2504.
7. Scardovelli Ruben, Zaleski Stéphane. Direct Numerical Simulation of Free-Surface and Interfacial Flow. *Annual Review of Fluid Mechanics*. 1999;.
8. Hirt C. W., Nichols B. D.. Volume of fluid (VOF) method for the dynamics of free boundaries. *Journal of Computational Physics*. 1981;.
9. Rider William J., Kothe Douglas B.. Reconstructing Volume Tracking. *Journal of Computational Physics*. 1998;.
10. Pavlidis Dimitrios, Gomes Jefferson L. M. A., Xie Zhihua, Percival James R., Pain Christopher C., Matar Omar K.. Compressive advection and multi-component methods for interface-capturing. *International Journal for Numerical Methods in Fluids*. 2016;80(4):256–282.
11. Shin Seungwon, Chergui Jalel, Juric Damir, Kahouadji Lyes, Matar Omar K., Craster Richard V.. A hybrid interface tracking – level set technique for multiphase flow with soluble surfactant. *Journal of Computational Physics*. 2018;359:409–435.
12. Soligo Giovanni, Roccon Alessio, Soldati Alfredo. *Acta Mech.*. 2019;230:683-696.
13. Herrmann M. A sub-grid surface dynamics model for sub-filter surface tension induced interface dynamics. *Computers and Fluids*. 2013;87:92–101.
14. Salinas P, Pavlidis D, Xie Z, Pain C C, Jackson M D. A Double Control Volume Finite Element Method with Dynamic Unstructured Mesh Optimization. *SPE Reservoir Simulation Conference*. 2017;:7.
15. Via-Estrem Lluís, Salinas Pablo, Xie Zhihua, et al. Robust control volume finite element methods for numerical wave tanks using extreme adaptive anisotropic meshes. *International Journal for Numerical Methods in Fluids*. ;.
16. Jackson Matthew D, Gomes J. Reservoir Modeling for Flow Simulation Using Surfaces , Adaptive Unstructured Meshes and Control-Volume-Finite-Element Methods. *SPE Reservoir Simulation Symposium*. 2013;:1–20.
17. Salinas P, Percival J R, Pavlidis D, et al. A Discontinuous Overlapping Control Volume Finite Element Method for Multi-Phase Porous Media Flow Using Dynamic Unstructured Mesh Optimization. *SPE Reservoir Simulation Symposium*. 2015;m.
18. Yang P, Xiang J, Fang F, Pavlidis D, Latham J.-P., Pain C C. Modelling of fluid–structure interaction with multiphase viscous flows using an immersed-body method. *Journal of Computational Physics*. 2016;321:571–592.
19. Obeysekera A, Lei Q, Salinas P, et al. Modelling stress-dependent single and multi-phase flows in fractured porous media based on an immersed-body method with mesh adaptivity. *Computers and Geotechnics*. 2018;103:229–241.
20. Xie Zhihua, Pavlidis Dimitrios, Percival James R., Gomes Jefferson L.M.A., Pain Christopher C., Matar Omar K.. Adaptive unstructured mesh modelling of multiphase flows. *International Journal of Multiphase Flow*. 2014;67:104 - 110. A Collection of Papers in Honor of Professor G. Hewitt on the Occasion of his 80th Birthday.
21. Xie Zhihua, Pavlidis Dimitrios, Salinas Pablo, Percival James R., Pain Christopher C., Matar Omar K.. A balanced-force control volume finite element method for interfacial flows with surface tension using adaptive anisotropic unstructured meshes. *Computers and Fluids*. 2016;138:38–50.

22. Pavlidis Dimitrios, Xie Zhihua, Percival James R., Gomes Jefferson L.M.A., Pain Christopher C., Matar Omar K.. Two- and three-phase horizontal slug flow simulations using an interface-capturing compositional approach. *International Journal of Multiphase Flow*. 2014;67:85 - 91. A Collection of Papers in Honor of Professor G. Hewitt on the Occasion of his 80th Birthday.
23. Cotter C J, Ham D A, C.C Pain. A mixed discontinuous/continuous finite element pair for shallow-water ocean modelling. *Ocean Modelling*. ;26:86–90.
24. Balay Satish, Gropp William D., McInnes Lois Curfman, Smith Barry F.. Efficient Management of Parallelism in Object-Oriented Numerical Software Libraries:163–202. Boston, MA: Birkhäuser Boston 1997.
25. Saad Youcef, Schultz Martin H. GMRES: A Generalized Minimal Residuals Algorithm for Solving Nonsymmetric Linear Systems. *Math. Comput.* 1983;44:417–424.
26. Henson Van Emden, Yang Ulrike Meier. BoomerAMG: A parallel algebraic multigrid solver and preconditioner. *Applied Numerical Mathematics*. 2002;41(1):155 - 177. Developments and Trends in Iterative Methods for Large Systems of Equations - in memorium Rudiger Weiss.
27. Smagorinsky J.. General circulation experiments wiht the primitive equations I. The basic experiment. *Monthly Weather Review*. 1963;.
28. Tezduyar T E. Stabilized Finite Element Formulations for Incompressible Flow Computations††This research was sponsored by NASA-Johnson Space Center (under grant NAG 9-449), NSF (under grant MSM-8796352), U.S. Army (under contract DAAL03-89-C-0038), and the University of Paris VI.. In: *Advances in Applied Mechanics*, vol. 28: Elsevier 1991 (pp. 1–44).
29. Pain Christopher C, Oliveira Cassiano R E, Goddard Antony J H, Umpleby Adrian P. Criticality Behavior of Dilute Plutonium Solutions. *Nuclear Technology*. 2001;135(3):194–215.
30. Hughes Thomas J R, Mallet Michel. A new finite element formulation for computational fluid dynamics: IV. A discontinuity-capturing operator for multidimensional advective-diffusive systems. *Computer Methods in Applied Mechanics and Engineering*. 1986;58(3):329–336.
31. Maddison J. R., Marshall D. P., Pain C. C., Piggott M. D.. Accurate representation of geostrophic and hydrostatic balance in unstructured mesh finite element ocean modelling. *Ocean Modelling*. 2011;39(3-4):248–261.
32. Pain CC, Umpleby AP. Tetrahedral mesh optimisation and adaptivity for steady-state and transient finite element calculations. *Computer Methods in Applied Mechanics and Engineering*. 2001;190:3771–3796.
33. Peraire Jaime, Vahdati Morgan, Morgan Ken, Zienkiewicz Olgierd C. Adaptive remeshing for compressible flow computations. *Journal of computational physics*. 1987;72(2):449–466.
34. Piggott Matthew, Farrell P.E., Wilson C.R., Gorman G.J., Pain C.C.. Anisotropic mesh adaptivity for multi-scale ocean modelling. *Philosophical Transactions of the Royal Society of London A: Mathematical, Physical and Engineering Sciences*. 2009;367(1907):4591–4611.
35. Alauzet Frédéric, Loseille Adrien. A decade of progress on anisotropic mesh adaptation for computational fluid dynamics. *Computer-Aided Design*. 2016;72:13–39.
36. Hiester H. R., Piggott M. D., Farrell P. E., Allison P. A.. Assessment of spurious mixing in adaptive mesh simulations of the two-dimensional lock-exchange. *Ocean Modelling*. 2014;73:30–44.
37. Löhner Rainald. Robust, Vectorized Search Algorithms for Interpolation on Unstructured Grids. *Journal of Computational Physics*. 1995;118(2):380–387.
38. Farrell PE, Maddison JR. Conservative interpolation between volume meshes by local Galerkin projection. *Computer Methods in Applied Mechanics and Engineering*. 2011;200(1-4):89–100.

39. Geuzaine Christophe, Meys B, Henrotte F, Dular P, Legros Willy. A Galerkin projection method for mixed finite elements. *IEEE transactions on magnetics*. 1999;35(3):1438–1441.
40. Wilson Cian. Modelling multiple-material flows on adaptive unstructured meshes. PhD thesis Imperial College London 2009.
41. Taylor Geoffrey. The Instability of Liquid Surfaces when Accelerated in a Direction Perpendicular to their Planes. I. *Proceedings of the Royal Society of London. Series A, Mathematical and Physical Sciences*. 1950;201(1065):192–196.
42. Sharp D. H.. An overview of Rayleigh-Taylor instability. *Physica D: Nonlinear Phenomena*. 1984;.
43. Jain Suhas S., Mani Ali, Moin Parviz. A conservative diffuse-interface method for compressible two-phase flows. *Journal of Computational Physics*. 2020;418:109606.
44. Xie Zhihua, Pavlidis Dimitrios, Percival James R., Gomes Jefferson L.M.A., Pain Christopher C., Matar Omar K.. Adaptive unstructured mesh modelling of multiphase flows. *International Journal of Multiphase Flow*. 2014;67:104 - 110. A Collection of Papers in Honor of Professor G. Hewitt on the Occasion of his 80th Birthday.
45. Tryggvason Grétar. Numerical simulations of the Rayleigh-Taylor instability. *Journal of Computational Physics*. 1988;75(2):253 - 282.
46. Guermond J.-L., Quartapelle L.. A Projection FEM for Variable Density Incompressible Flows. *Journal of Computational Physics*. 2000;165(1):167 - 188.
47. Ding Hang, Spelt Peter D.M., Shu Chang. Diffuse interface model for incompressible two-phase flows with large density ratios. *Journal of Computational Physics*. 2007;226(2):2078 - 2095.
48. Waddell J. T., Niederhaus C. E., Jacobs J. W.. Experimental study of Rayleigh–Taylor instability: Low Atwood number liquid systems with single-mode initial perturbations. *Physics of Fluids*. 2001;13(5):1263-1273.
49. Geuzaine Christophe, Remacle Jean François. Gmsh: A 3-D finite element mesh generator with built-in pre- and post-processing facilities. *International Journal for Numerical Methods in Engineering*. 2009;.
50. Lee Hyun Geun, Kim Junseok. Numerical simulation of the three-dimensional Rayleigh–Taylor instability. *Computers & Mathematics with Applications*. 2013;66(8):1466–1474.
51. Mayor T. S., Ferreira V., Pinto A. M.F.R., Campos J. B.L.M.. Hydrodynamics of gas-liquid slug flow along vertical pipes in turbulent regime-An experimental study. *International Journal of Heat and Fluid Flow*. 2008;29(4):1039–1053.
52. Kampitsis A E, Adam A, Salinas P, Pain C C, Muggeridge A H, Jackson M D. Dynamic adaptive mesh optimisation for immiscible viscous fingering. *Computational Geosciences*. 2020;24(3):1221–1237.

How to cite this article: Obeysekara A., P. Salinas, C.E. Heaney, L. Kahouadji, L. Via-Estrem, J. Xiang, N. Srinil, A. Nicolle, O.K. Matar, and C.C. Pain (2020), Prediction of high aspect ratio multiphase flows using anisotropic mesh optimisation, XX, XX.